Materials Views
www.MaterialsViews.com

ADVANCED OPTICAL MATERIALS
www.advopticalmat.de

FULL PAPER

Hierarchical Electrohydrodynamic Structures for Surface-Enhanced Raman Scattering

*Pola Goldberg-Oppenheimer, Sumeet Mahajan, and Ullrich Steiner**

Surface enhanced Raman scattering (SERS) is a well-established spectroscopic technique that requires nanoscale metal structures to achieve high signal sensitivity. While most SERS substrates are manufactured by conventional lithographic methods, the development of a cost-effective approach to create nanostructured surfaces is a much sought-after goal in the SERS community. Here, a method is established to create controlled, self-organized, hierarchical nanostructures using electrohydrodynamic (HEHD) instabilities. The created structures are readily fine-tuned, which is an important requirement for optimizing SERS to obtain the highest enhancements. HEHD pattern formation enables the fabrication of multiscale 3D structured arrays as SERS-active platforms. Importantly, each of the HEHD-patterned individual structural units yield a considerable SERS enhancement. This enables each single unit to function as an isolated sensor. Each of the formed structures can be effectively tuned and tailored to provide high SERS enhancement, while arising from different HEHD morphologies. The HEHD fabrication of sub-micrometer architectures is straightforward and robust, providing an elegant route for high-throughput biological and chemical sensing.

1. Introduction

Surface-enhanced Raman scattering (SERS) is an extremely sensitive molecular finger-printing technique which can detect chemical substances down to the single molecule level[1,2] with important applications in forensics, healthcare, and diagnostics. SERS is based on the electromagnetic field enhancement by localized optical fields (surface plasmon polaritons or, simply, plasmons) on nanostructured metallic structures.[3,4] Localized plasmon resonances can be tuned by manipulation of the surface architecture at the sub-micrometer level, giving rise to the huge Raman signal enhancements SERS is known for. Hence, controlled surface fabrication techniques underpin the development of next-generation plasmon-active devices such as those used in SERS. The development of a robust, cost-effective and simple technique that enables the design and construction of well-controlled large area surface structures with mesoscopic lengths scales is therefore essential to enable progress in plasmonic devices.

The vast majority of earlier synthetic routes to generate SERS structures with suitable reproducibility are based on conventional lithographic techniques.[5] These are not only expensive and time consuming but are also often cumbersome and require precise integration of multistep processes, thus limiting the scalability of the resulting structures. For instance, while photolithography[6] is a flexible method for generating optical patterns, it is limited by the optical diffraction limit and is essentially 2D, meaning that many steps must be iterated to create a 3D structure. Electron beam lithography is an alternative approach that uses a scanning beam of electrons[7] to write sub-micrometer structures into a resist that can subsequently be transferred to the substrate material, often by etching. The preparation of such patterns not only requires sequential writing steps, but is also vulnerable to beam drift or instability which may occur during the long exposure times. Limited resolution, poor mechanical stability of the mould, and pattern distortion are the limiting factors of microlithography and other imprinting techniques.[8,9] Alternative routes for multiscale structures include self-assembly[10] or biomimetic processes,[11] but, the precise control of features and prevention of defects remain a challenge, particularly in the sub-micrometer regime. The limits of the above-mentioned top-down approaches and self-assembly based bottom-up approaches highlight the need for more reliable, cost-effective, and straightforward patterning methods to develop tunable 3D structures.

Here, we report an approach that addresses some of the problems described above, and enables the formation of hierarchical 3D structures with three independent, characteristic lateral dimensions. Hierarchical electrohydrodynamic (HEHD) pattern formation harnesses sequential instabilities in multilayer thin films induced by an electric field to guide the layer material into design structures, allowing different materials to be patterned in a one-step procedure. HEHD offers a great variability of structural features by the independent control of several parameters. Hierarchical polymer structures covered by a plasmon-active-metal (in this case gold) effectively enhance the EM field leading to high SERS enhancements.

The background of electrohydrodynamic (EHD) instabilities has been described in detail in a number of publications.[12–15] In brief, the physical principle of EHD instabilities is based on

Dr. P. Goldberg-Oppenheimer, Dr. S. Mahajan,
Prof. U. Steiner
Department of Physics
Cavendish Laboratory
University of Cambridge
J J Thomson Avenue, Cambridge CB3 0HE, UK
E-mail: u.steiner@phy.cam.ac.uk

DOI: 10.1002/adma.201104159

subjecting initially homogeneous dielectric films to an electric field. This field gives rise to a destabilizing electrostatic pressure p_{el} at the interface between the liquid dielectric and air, which arises from the coupling of the interfacial displacement charges to the electric field. This pressure couples to the capillary wave spectrum of the liquid interface, overcoming the compensating surface tension γ, thereby amplifying interface undulations with a characteristic wavelength

$$\lambda_{\max} = 2\pi\sqrt{\frac{2\gamma}{-\partial p_{el}/\partial h}} = 2\pi\sqrt{\frac{\gamma U}{\varepsilon_0 \varepsilon_p (\varepsilon_p - 1)^2}}\, E_f^{-3/2} \tag{1}$$

where h is the film thicknesses of liquid layer with dielectric constant ε_p, ε_0 is the dielectric permittivity of vacuum, and U is the voltage applied to the capacitor giving rise of the electric field in the film E_f. The instability develops over a time τ which scales linearly with the viscosity η, inversely with γ, and is proportional to the fourth power of the dominantly growing wavelength:

$$\tau = \frac{3\eta\lambda^4}{(2\pi)^4 \gamma h^3} \tag{2}$$

The amplification of a narrow band of wavelengths drains the surrounding dielectric film, laterally detaching the individual surface structures which evolve into pillar arrays.

2. Results and Discussion

The EHD patterning process is very well understood for single liquid layers and polymer bilayers.[16] Here, we have applied this principle to polymer trilayers in our HEHD approach. The structure formation in a multilayer film can be controlled by carefully designing the layer sequence. In a polymer(P_1)–polymer(P_2)–polymer(P_3)–air trilayer (**Figure 1**a), a careful selection of polymers inhibits uncontrolled dewetting of the multilayer allowing control over the sequential destabilization of the trilayer assembly in a layer-by-layer fashion. To this end, the trilayer is assembled according to the glass transition temperatures T_g of the individual layers, starting from the highest T_g for the bottom film to the lowest T_g for the top-most layer (i.e., $T_{g1} > T_{g2} > T_{g3}$). This way, each layer can be liquefied individually while preserving the underlying layer in a stable state. The resulting hierarchical architecture is an outcome of the sequential electrostatic destabilization of the stack, schematically shown in Figure 1. Heating at $T_{g3} < T < T_{g2}$ at constant applied potential U results in the destabilization of the upper layer, forming pillars which span from the film surface to the upper electrode (Figure 1a,b). The primary pillar formation of P_3 paves the way for the deformation of the intermediate layer at the P_2–P_3 contact line, where electrostatic forces are the highest. Raising the temperature to $T_{g2} < T < T_{g1}$ while keeping the potential applied drives a flow of P_2 to the upper electrode along the outside of the P_3 column (Figure 1b,c). This generates a P_2 mantle surrounding the P_3 primary column. Upon completion of the secondary instability, T_g is further raised to $T > T_{g1}$ generating a third instability in P_1. Again, the liquified material of P_1 flows upwards around the secondary P_2 cylinder (Figure 1c,d).

While the applied electric field stabilizes the coaxial column morphology, wetting properties of the three materials come into play once the composite columns have formed, typically leading to a break-up of the coaxial layers. It is therefore advantageous to organize the polymer sequence according to their surface tension (i.e., $\gamma_1 < \gamma_2 < \gamma_3$), which additionally stabilizes the final coaxial structure. Furthermore, grouping the three materials in order of increasing viscosities (e.g., $\eta_1 < \eta_2 < \eta_3$) minimizes the pattern formation time while enhancing pattern stability.

The triple layer consisted of ethyl cellulose (EC), polyvinyl alcohol (PVA), and polyvinyl acetate (PVAc) which were sequentially deposited. This layer had the required parameters as listed above, with $T_{EC} > T_{PVA} > T_{PVAc}$, $\gamma_{EC} < \gamma_{PVA} < \gamma_{PVAc}$, and $\eta_{EC} < \eta_{PVA} \approx \eta_{PVAc}$. A slight misalignment of the capacitor plates gave rise to wedge geometry with a variation in plate spacing d ranging from 100 nm to 1 µm across the 1 cm wide sample. As the temperature is increased, the interfaces are destabilized at different times leading to a sequential lateral redistribution of all three materials. The wedge geometry causes predominantly a variation in τ, affecting λ only very little.[17] This enables the visualisation of different stages of the instability on a single sample. Initially, the film develops low-amplitude undulations (**Figure 2**b, right hand side), which are further amplified and eventually span the two electrodes forming an array of liquid pillars with local (and sometimes global) hexagonal symmetry (Figure 2b, left). Figure 2b shows an intermediate stage of this process, with the variation from undulations (right) to column formation (left) stemming from the wedge geometry of the

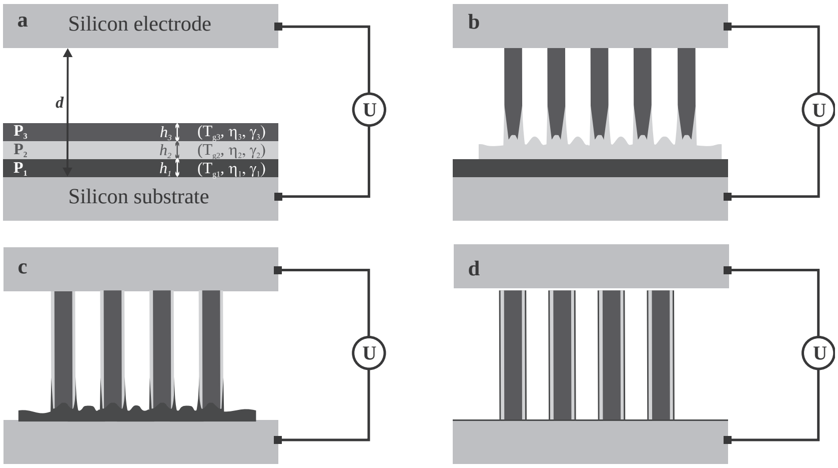

Figure 1. Mechanism of the HEHD structure formation process. a) The initially assembled polymer trilayer is destabilized by applying a voltage U. b) The primary instability yields pillars which span the capacitor gap. A secondary instability arises from a deformation in P_2 at the P_2–P_3 contact line caused by primary P_3 pillar formation. The amplification of the secondary instability guides P_2 upwards forming a shell surrounding the P_3 column. c) Similarly, a third instability takes place in P_1 which is drawn upwards to form a second mantle around the pillar. d) The final configuration consists of a core–shell$_2$–shell$_1$ structure comprised of a primary P_3 pillar coated concentrically by P_2 and P_1.

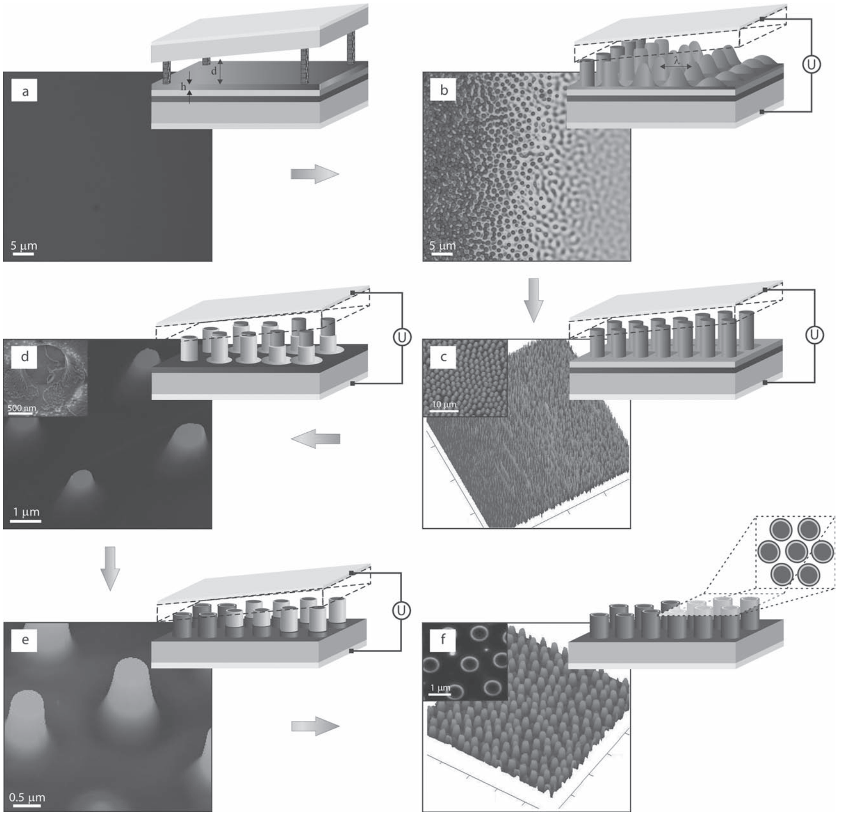

Figure 2. Sequential HEHD patterning steps. a) Optical micrograph of the initial EC–PVA–PVAc three-layer stack. b) Surface instability in the PVAc upper layer upon heating above T_{g3} and applying a voltage U. The electrode wedge geometry causes the instability to sweep across the sample revealing different instability stages, from early undulations with a characteristic wavelength (right) to columns spanning the capacitor gap (left). c) AFM image of fully formed PVAc columns. Raising the temperature above the T_g of PVA causes a secondary instability forming a mantle surrounding the primary PVAc columns (inset: SEM image). e) A further rise in temperature softens the bottom EC film, giving rise to a second mantle around the columns. The 3D AFM image in (f) reveals a pillar array consisting of three concentric cylinders shown in the optical micrograph in the inset.

bounding electrodes. This eventually leads to the cylindrical columns shown in Figure 2c. These formed structures have a continuous variation of aspect ratio along the wedge-shaped cell. A representative atomic force microscopy (AFM) image revealing the lateral variation in pillar aspect ratio is shown in Figure 2c. These primary pillar structures therefore lend themselves to study and optimization of SERS substrates in a combinatorial manner.

In order to evaluate the SERS performance of HEHD patterned structures shown in Figure 2c, they were coated with 20 nm thick gold layer (see Supporting Information (SI) for roughness and thickness details). A scanning electron microscopy (SEM) and transmission electron microscopy (TEM) analyses on the uncoated and gold-coated structures confirmed smooth and conformal coverage of HEHD generated structures (see SI, Figure S4). This was followed by adsorption of a benzenethiol monolayer by dipping the gold coated surfaces in its 10 mM ethanolic solution. The SERS spectra recorded for these pillar-like single column structures are shown in **Figure 3**a. In addition to averaged spectroscopic data, SERS mapping was carried out for the pillar array. A representative SERS map overlaid over the corresponding optical image is shown in Figure 3b. Even though the gold coating was homogeneously deposited onto the surface, the SERS signal (white) comes only from the EHD pillars. No SERS signal is observed from the flat sputtered gold (Figure 3a, thickness 0.0) and also from in between the pillars in Figure 3b. A comparison of SERS spectra from different sample locations in Figure 3a shows the effect of the electrode wedge geometry, which results in a continuous variation of the pillar aspect ratio. For 633 nm laser excitation, single pillars with an aspect ratio 0.79 gave nearly 30-times enhanced SERS signal compared to the lowest aspect ratio of 0.61. A similar trend was obtained in the near-infrared (785 nm) with high signals obtained for highest aspect ratios. Note that the SERS of Figure 3a arises almost exclusively from a single column. The adjacent columns are not plasmonically coupled to each other

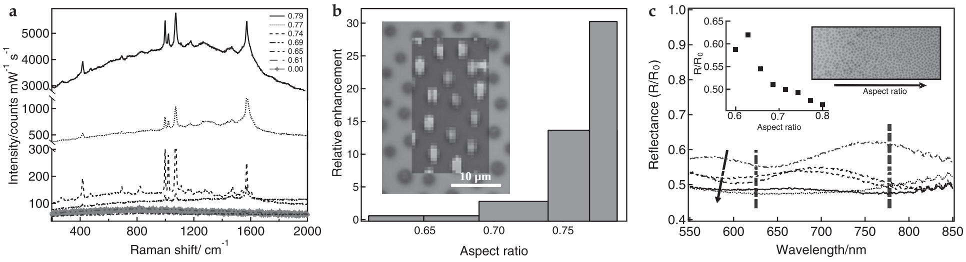

Figure 3. SERS signal versus pillar aspect ratio. a) SERS spectra of benzenethiol recorded from substrates with pillars of various aspect ratios excited with a 785 nm laser. b) The relative SERS enhancement increases strongly with the aspect ratio. The inset shows a SERS map overlaid over an optical image of the patterned area, revealing the localised nature of the SERS activity extracted for the benzenethiol peak at 1070 cm^{-1}. c) Reflectance spectra (acquired at the same locations as in (a) for pillars with different aspect ratios. The dashed lines indicate the excitation wavelengths of 633 and 785 nm. The left inset shows the variation in reflectance at 785 nm. The right inset shows an optical image of the pillar array. The color change across the sample arises from the variation in aspect ratio.

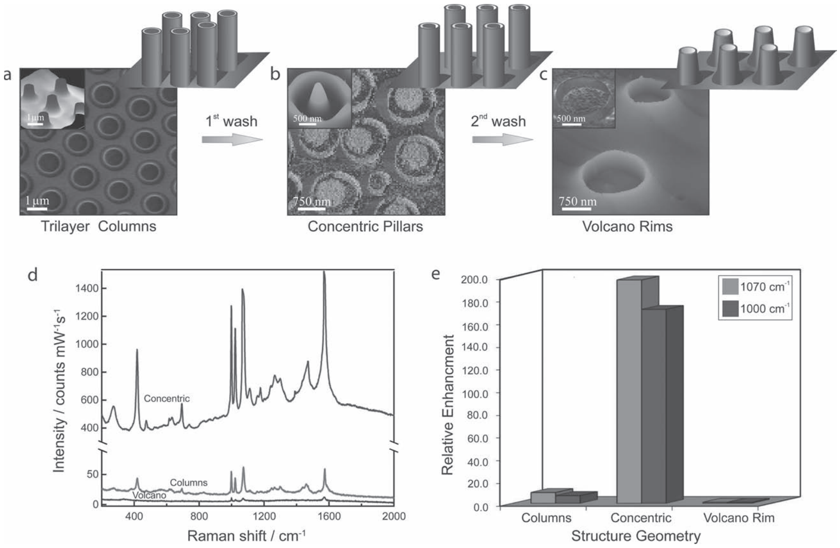

Figure 4. Manufacture of hierarchical architectures. AFM and SEM images of structures derived from the trilayer coaxial pillars in (a) following sequential washing steps: b) central PVAc pillars surrounded by thin EC rims, and c) EC nanovolcanos. d) SERS of benzenethiol on the three HEHD-structured surfaces. The highest signal enhancement was obtained for the concentric pillar-rim structure in (b). e) Relative SERS enhancement of the 1000 cm^{-1} and 1070 cm^{-1} peaks.

unlike some other submicrometer SERS structures.[18] HEHD patterned individual pillars therefore function as isolated detection centres, rendering these patterned substrates as possible platforms for multiplexed SERS of different chemical species.

Figure 3c shows the spectrally resolved reflectance across a sample consisting of columns with laterally varying aspect ratios (inset). The reflectance spectra shows increasing extinction at the pump excitation of 633 and 785 nm (dashed lines) with increasing pillar aspect ratio. The (left) inset shows this variation at 785 nm, with a nearly 30% increase in extinction when varying the aspect ratio from 0.6 to 0.8. This extinction primarily arises from coupling of light into plasmon resonances which are tuned by the pillar geometry. This shows that the relative SERS enhancement of Figure 3a is correlated with the increased strength of plasmonic coupling into the structure as shown in Figure 3c. The tuneability of the aspect ratio and its effect on strength of plasmon resonances and SERS allows the optimization of substrates for different laser excitation wavelengths.

Going beyond simple pillar arrays, hierarchical structures were formed by enabling a secondary instability in the PVA layer once the PVAc columns have fully formed (Figure 2c). The electrostatic pressure gradient at the surface of the primary columns drives the flow of the underlying PVA layer upwards along the PVAc pillars, forming a thin, ≈170 nm-wide shell enclosure around the inner cylindrical core column (diameter: ≈750 nm). Again, various intermediate stages of PVA shell heights can be obtained on a single sample caused by the lateral field variation arising from the wedge geometry of the electrodes (Figure 2d). Similarly a third instability can be triggered by liquefying the lowest EC layer (Figure 2e) following the completion of the coaxial pattern of the upper bilayer. Hierarchical structures with a cylindrical PVAc core surrounded by a mantle of PVA and a second shell of EC were created in this fashion. The overall diameter of a trilayer concentric pillar was 1.09 ± 0.10 µm, with an average height of 771 ± 8.00 nm.

Once the hierarchical pillars have fully formed (**Figure 4**a), a variety of multiscale structures can be realized by dissolving some of the three polymers. Pillars surrounded by a concentric shell were created by washing out the intermediate PVA with a non-solvent (i.e., distilled water) for the PVAc and EC. This resulted in primary columns of PVAc with a typical diameter of 750 ± 21 nm, surrounded by a thin rim of EC with a wall thickness of only 87 ± 13 nm (Figure 4b). The gap width between the pillar and the free-standing shell was 170 ± 29 nm (Figure 4b,c). The amount of a EC covering the bottom of the gap with respect to the material driven into the EC rim depends on the interplay of wetting and electrostatic driving force and the kinetics of rim formation. In the present experiments the height of the EC rim was typically lower than that of the central cylinder (Figure 4b, inset). An additional washing step removes the central column and leaves behind EC volcano rims (Figure 4c, inset) with a width of only 87 nm, considerably smaller than the width of the primary PVAc column. Hence, HEHD patterning enables the generation of sub-100 nm features that are arranged in a lateral array. Again, the electrode wedge geometry generates a range of structural rim parameters.

The detailed control over the column morphology and their aspect ratio offered by HEHD patterning provides interesting substrates for SERS. To this end, a 20 nm-thick gold layer was evaporated onto the various polymer structures and coated with a monolayer of benzenethiol molecules. Different HEHD morphologies gave substantial variations in SERS enhancements (Figure 4d). The flat part of the samples with just the sputtered gold layer as well as reference samples with just gold coated on polymer surfaces did not give any SERS signals. This confirms that HEHD patterned structures are indeed solely responsible for any observed SERS enhancements. The concentric pillar-rim structure showed a 25× enhancement compared to simple pillars and a nearly 200-fold increase in signal over the volcano rim structure at an excitation wavelength of 785 nm (Figure 4e). This difference in SERS signal was less dramatic at 633 nm, with simple pillars and the concentric pillar-rim structure showing similar signals and the volcano structures showing a ≈ 5× lower signal (see SI). The absolute enhancement for the concentric pillar-rim SERS substrate was ~1.0×10^7 at 785 nm and 1.5×10^6 at 633 nm. We find the 0.95 confidence intervals to be (8.24×10^6, 1.18×10^7) and (1.43×10^6, 1.57×10^6), respectively. An enhancement of 1.2×10^6 with a 95% confidence interval of (1.15×10^6, 1.25×10^6) was found for simple columns at 633 nm. Note that these enhancement factors are normalized by illuminated area (spot size) while the SERS activity is localized at the surface structure and therefore stems only from a small fraction of the sample area. The performance of our substrates compares favourably with enhancements on Klarite,[19] a commercially available substrate. The enhancement was found almost similar in magnitude, although surprisingly, with both 785 and 633 nm lasers. With the 785 nm laser Klarite gave an enhancement of 1.2×10^7 and at 633 nm it gave an enhancement of 1.4×10^6 under our experimental conditions. Theoretical modelling could help further improve our EHD structures and the enhancements that can be obtained from them and this is currently underway.

3. Conclusion

In conclusion, a straightforward hierarchical electrohydrodynamic pattern-formation technique was used to produce well-defined sub-micrometer architectures in a tunable manner. Secondary and ternary EHD instabilities result in rim-patterns with widths that are one order of magnitude smaller than the primary columns. The generated structures display plasmonic properties which are controlled by the HEHD patterning parameters. This tunability allows the patterned substrates to be optimized for plasmon-dependent phenomena and, indeed, the different HEHD patterns show structure dependent SERS. For optimized columns surrounded by coaxial rims, a 1.0×10^7 SERS enhancement was observed. Since this SERS enhancement arises from each of the isolated structures in the array, HEHD patterned surfaces are an ideal platform for multiplexed SERS detection, where each of the individual HEHD structures can be used to detect a different molecular species. In addition our results of being able to form large area reproducible sub-micrometer tunable plasmonic structures opens up a range of further possible implementations in areas such as photocatalysis, photovoltaics, and bioanalytics.

4. Experimental Section

Polyvinyl acetate (PVAC), polyvinyl alcohol (PVA; Sigma-Aldrich), and ethyl cellulose (EC; Fluka), were used without further purification. Highly polished *p*-doped silicon wafers, with (100) crystal orientation (Wafernet GmbH, Eching, Germany) were used as substrates.

Prior to spin-coating, the substrates were cleaned in a 'Piranha' solution consisting of 3:1 H_2SO_4 (98%):H_2O_2 (30%), followed by thorough rinsing with deionised water and drying under nitrogen. The ITO-coated glass slides were cleaned by scrubbing in soap water at 75 °C and washing in an ultrasonic bath with acetone and isopropanol, followed by irradiation for 20–30 min in a UV–ozone cleaner. Immediately before device assembly, all substrates and electrodes were subjected to snowjet cleaning.

First, a thin film of EC ($\gamma = 28.5$ mN m^{-1}, $T_g = 130$ °C, $\eta = 0.084$ Pa s), 150 nm in thickness, was spin-coated onto a freshly cleaned Si substrate from toluene. A 110 nm layer of PVA ($\gamma = 50$ mN m^{-1}, $T_g = 85$ °C, $\eta = 0.073$ Pa s) was then spin-coated directly on top of the EC film from water solution to form an EC/PVA bilayer. Water is a nonsolvent for EC. PVAc ($\gamma = 57.8$ mN m^{-1}, $T_g = 30$ °C, $\eta = 0.225$ Pa s) was spin cast from toluene onto a glass slide and the resulting 100 nm thick film was floated onto a pool of deionized water and transferred onto the PVA layer to form an EC/PVA/PVAc trilayer. The sample was subsequently placed into a vacuum oven to remove the residual water.

A capacitor set-up was assembled using the trilayer covered substrate as one of the electrodes. Facing it, a second silicon wafer was mounted, leaving a thin air gap. The overall electrode spacing, *d* was adjusted by using lithographically prepared spacers or silicon oxide colloids as spacers. The backsides of the both electrodes were coated with a thin gold layer (h = 100 nm) followed by electrically contacting them using silver paste (Electrodag 1415M). The films were sequentially liquefied by thermal heating, raising the temperature above the T_g of each the resist, and a voltage of 80 V was applied to the capacitor device. The experiment was terminated by quenching the assembly to room temperature before removing the electric field. The top electrode was removed and and some of the polymers were selectively dissolved. PVA was removed by dissolution in distilled water which is a nonsolvent for both the EC and PVAc. Cycloheptane or cyclopentane were used to dissove the central PVAc column without removing the EC rim.

The evolving patterns were observed with a standard optical microscope (Olympus BX 40) and an inverted reflective optical microscope (Olympus GX61) operated in clean-room conditions. Digital cameras connected to both microscopes were read out by imaging software (Carl Zeiss Visiocam). A NanoScope IV Multimode Dimension 3100 AFM was used to quantitatively determine the sample topography. Height and phase images were analyzed using the Nanoscope software (Digital Instruments). The AFM measurements yielded the film thickness *h*, the plate spacing *d*, the characteristic wavelength λ, and the width and height (i.e., aspect ratios) of the generated patterns. Optical and AFM micrographs showed the lateral distribution of the patterned polymers on the substrate. The SEM measurements were performed using a LEO ULTRA 55 SEM including a Schottky emitter (ZrO/W cathode) at acceleration voltages of 5.0–10.0 kV with a lateral resolution of 2–5 nm.

The HEHD substrates were covered with a thin Au film using an Emitech sputter-coater with a DC Ar plasma (gold target purity 99.999% supplied by Kurt J. Lesker Company). The gold was deposited to approximately 20 nm as per the calibration of the sputter coater (current vs deposition rate). Accordingly two cycles of 30 s at 70 mA were carried out (also see SI). The deposition was performed onto all of the EHD formed structures and onto polymer films as reference samples.

SERS measurements were carried out with an InVia Renishaw Raman Microscope System equipped with 633 and 785 nm lasers. The spectra were typically acquired with a 10 s exposure time and a laser power of 3 and 10 mW at the sample at 633 nm and 785 nm, respectively. SERS maps were acquired in Streamline mode (line scan) with 20 s exposure time and 6 and 100 mW power at 633 and 785 nm, respectively. A 50× objective with a numerical aperture of 0.75 was used for all measurements. Optical measurements were carried out with an Olympus BX51 microscope equipped with an incoherent white light (halogen) source and an optical fibre coupled to a QE65000 Ocean Optics spectrometer. The spectra were normalized with respect to those recorded on flat gold.

Acknowledgements

This work was funded by Kodak European Research, Cambridge and by the EPSRC (EP/G060649/1 and EP/H028757/1).

Received: October 28, 2011
Revised: December 29, 2011

---

[1] K. Kneipp, Y. Wang, H. Kneipp, L. T. Perelman, I. Itzkan, R. R. Dasari, M. S. Feld, *Phys. Rev. Lett.* **1997**, *78*, 1667–1670.
[2] S. Nie, S. R. Emory, *Science* **1997**, *275*, 1102–1106.
[3] W. L. Barnes, A. Dereux, T. W. Ebbesen, *Nature* **2003**, *424*, 824–830.
[4] E. Ozbay, *Science* **2006**, *311*, 189–193.
[5] N. M. Perney, J. J. Baumberg, M. E. Zoorob, M. D. B. Charlton, S. Mahnkopf, C. M. Netti, *Opt. Express* **2006**, *14*, 847–857.
[6] E. Menard, M. A. Meitl, Y. G. Sun, J. U. Park, D. J. L. Shir, Y. S. Nam, S. Jeon, J. A. Rogers, *Chem. Rev.* **2007**, *107*, 1117–1160.
[7] M. Kahl, E. Voges, S. Kostrewa, C. Viets, W. Hill, *Sens. Actuators B* **1998**, *51*, 285–291.

[8] S. Y. Chou, P. R. Krauss, P. J. Renstrom, *Science* **1996**, *272*, 85–87.
[9] D. Qin, Y. N. Xia, J. A. Rogers, R. J. Jackman, X. M. Zhao, G. M. Whitesides, *Microsystem Technology in Chemistry and Life Science; Topics in Current Chemistry*, Vol. 194, Springer, UK **1998**, pp.1–20.
[10] B. Yan, A. Thubagere, W. R. Premasiri, L. D. Ziegler, L. Dal Negro, B. M. Reinhard, *ACS Nano* **2009**, *3*, 1190–1202.
[11] N. L. Garrett, P. Vukusic, F. Ogrin, E. Sirotkin, C. P. Winlove, J. Moger, *J. Biophotonics* **2009**, *2*, 157–166.
[12] A. Onuki, *Physica A* **1995**, *217*, 38.
[13] E. Schaffer, T. Thurn-Albrecht, T. P. Russell, U. Steiner, *Europhys. Lett.* **2001**, *53*, 518–524.
[14] L. F. Pease, W. B. Russel, *J. Chem. Phys.* **2003**, *118*, 3790–3803.
[15] L. F. Pease, W. B. Russel, *Langmuir* **2004**, *20*, 795–804.
[16] M. D. Morariu, N. E. Voicu, E. Schaffer, Z. Q. Lin, T. P. Russell, U. Steiner, *Nat. Mater.* **2003**, *2*, 48–52.
[17] P. Goldberg-Oppenheimer, U. Steiner, *Small* **2010**, *6*, 1248–1254.
[18] S. Mahajan, R. M. Cole, B. F. Soares, S. H. Pelfrey, A. E. Russell, J. J. Baumberg, P. N. Bartlett, *J. Phys. Chem. C* **2009**, *113*, 9284–9289.
[19] WEBSITE: www.renishawdiagnostics.com, accessed: October, 2011.